Environmental Science Nano

ROYAL SOCIETY OF CHEMISTRY

PAPER

View Article Online
View Journal | View Issue

Cite this: *Environ. Sci.: Nano*, 2024, **11**, 1271

Super stable evaporators based on upcycled self-healing adsorbents for wastewater regeneration†

Meng Li, ‡[a] Hongmin Guo,‡[a] Yumeng Xiao,[a] Sichen Liu,[a] Yifan Lu,[a] Lidong Wang*[a] and Tony D. James *[bc]

Received 15th November 2023,
Accepted 22nd January 2024

DOI: 10.1039/d3en00829k

rsc.li/es-nano

Interfacial evaporation systems have enormous potential for wastewater treatment and freshwater generation. However, a technological gap remains in achieving a sustainable solar-driven water purification system that combines rapid evaporation rates with enhanced stability. With this research, we investigated a self-healing water purification platform that incorporates cellulose nanocrystals that encapsulate polyaniline into a PVA–borax dynamic crosslinked network, which is capable of effectively enriching heavy metal ions and generating clean water. The wastewater regeneration system was developed to remove heavy metal ions through adsorption, then the hydrogel was recovered through self-healing for use as an interface evaporator for secondary purification of the wastewater. Combining an exhausted self-healing gel with different substrates using the self-adhesive properties, a dual-layer evaporator with excellent water evaporation performance was fabricated. A cotton thread evaporator achieved a high evaporation rate of 2.19 kg m^{-2} h^{-1} under 1 sun. Subsequent, purification of wastewater meets with the WHO drinking water standards following the adsorption–evaporation purification process. This strategy provides an efficient, green, and sustainable approach for achieving wastewater regeneration and heavy metal-free drinking water.

Environmental significance

Heavy metal pollution has exacerbated the global drinking water crisis, posing a threat to public health and the environment. Successful remediation and removal of heavy metal have been accomplished by adsorption-based materials. Specifically, we engineered a self-healing hydrogel for heavy metals removal and the exhausted adsorbents were then self-healed and upcycled as a solar steam evaporator for drinking water generation. COMSOL simulations also confirm the significant potential of the upcycled evaporator for practical water purification applications. Our waste-to-wealth strategy offers an innovative approach to environmental remediation with outstanding long-term stability, energy efficiency, and eco-friendliness, presenting a new perspective on wastewater recycling and its potential for mitigating water crises.

1. Introduction

Rapid industrial development has given rise to a severe energy crises and environmental issues, including water pollution and waste disposal.[1–6] Substantial effort has been devoted to waste-to-treasure strategies, thus minimizing energy consumption and environmental impact.[7–10] The conversion of waste into value-added chemicals such as the utilization of solar energy for wastewater purification is considered as a beneficial processes for resource utilization in an upgraded circular pathway.[11,12] The efficient harnessing of solar energy is crucial to address future energy and environmental challenges.[13,14] The waste–treating-waste strategy involves recycling and reusing depleted adsorbents as interface solar evaporators for secondary purification of wastewater.[15] However, the realization of resource recycling and upgrading of exhausted adsorbents poses an extremely high requirement on the mechanical and damage resistant properties of the materials.[16] The practical application of this method is limited by inherent constraints, particularly associated with the recyclability and operational lifecycle.[17]

[a] *Hebei Key Lab of Power Plant Flue Gas Multi-Pollutants Control, Department of Environmental Science and Engineering, North China Electric Power University, Baoding, 071003, P. R. China. E-mail: wld@ncepu.edu.cn*
[b] *Department of Chemistry, University of Bath, Bath, BA2 7AY, UK. E-mail: t.d.james@bath.ac.uk*
[c] *School of Chemistry and Chemical Engineering, Henan Normal University, Xinxiang 453007, P. R. China*

† Electronic supplementary information (ESI) available: Details for regent and materials. Figure and table of characterization results (SEM, zeta), experimental results related to the self-healing properties and interfacial photothermal evaporation performance and stability in harsh environment. COMSOL Multiphysics calculation configurations. See DOI: https://doi.org/10.1039/d3en00829k

‡ Indicates the co-first author.

During the process of adsorption and subsequent upcycling of adsorbents, it is inevitable that physical damage will occur (*e.g.*, erosion, cracks, fractures, and disintegration) due to water impact or human factors.[18,19] The gradual growth of small physical defects often leads to a reduction in the materials performance, ultimately resulting in equipment failure.[20,21] To enhance the mechanical stability, a "soft–hard synergistic" strategy can be employed whereby reinforcement materials are incorporated as rigid fillers into a soft amorphous matrix, resulting in a soft–hard dual-network structure.[22] Through the synergistic interplay between the rigid and soft components, material stress energy is dissipated significantly, thereby enhancing resistance to deformation and fracture. However, the contribution of this toughening method for improving mechanical performance is limited.[23] The introduction of self-healing hydrogel soft materials could enable autonomous repair of damage that may evolve into catastrophic failures.[24–26] Hydrogels prepared using dynamic interactions formed by boronic ester bonds exhibit high toughness, fatigue resistance, and excellent self-healing ability.[27,28] By incorporating boronic ester dynamic covalent bonds as the soft segments and introducing robust material nanocellulose (C-CNC) as the hard segments, a synergistic interaction between the soft and hard domains is created, resulting in a durable and tough self-healing material,[29,30] which exhibits significantly enhanced stability and recyclability of the hydrogel for both metal ion adsorption and subsequent evaporator fabrication.[31]

To further enhance the photothermal stability, a dual-layer evaporator was developed which offers the possibility of practical long-term use and record-high evaporation rates.[32] Through the synergistic effect of an upper layer structure and a lower layer structure with hydrophilic substrate for continuously water supply, a significant improvement in the evaporation rate was achieved.[33] However, the fabrication methods of such dual-layer evaporators, using 3D printing technologies, vacuum filtration deposition, and casting strategies, still face challenges in terms of complex manufacturing processes and high costs.[34–36] The combination of a self-healing photothermal layer and the water supply matrix in the dual-layer evaporator could be achieved by self-adhesion, ensuring a seamless, environmentally friendly, and stable structural integration.[37] Various substrates with excellent continuous water transport capability can be used for evaporator development in order to achieve high photothermal conversion efficiency with excellent stability.

Here, we present an energy-saving strategy for the treatment of complex contaminated wastewater, as shown in Fig. 1. A self-healing hydrogel with porous and extensive hydrogen bonding networks was synthesized using polyaniline as light-absorbing materials, carboxymethyl cellulose as the hard domain, and polyvinyl alcohol–borax as the soft thread. The synergistic effect of PVA soft thread and C-CNC–PANI mixed network with "soft and hard" combination imparted good mechanical properties to the hydrogel. Meanwhile, the chemically cross-linked dynamic covalent bonds and multiple hydrogen bonds endowed the hydrogel with rapid self-healing capability. The resulting hydrogel was first subjected to an adsorption process to remove heavy metal ions, after which the gel is recovered and self-healed. By virtue of the gel's excellent self-adhesive properties, it can be composited with different water-transport substrates to fabricate evaporators for secondary water purification, thereby achieving the transformation of

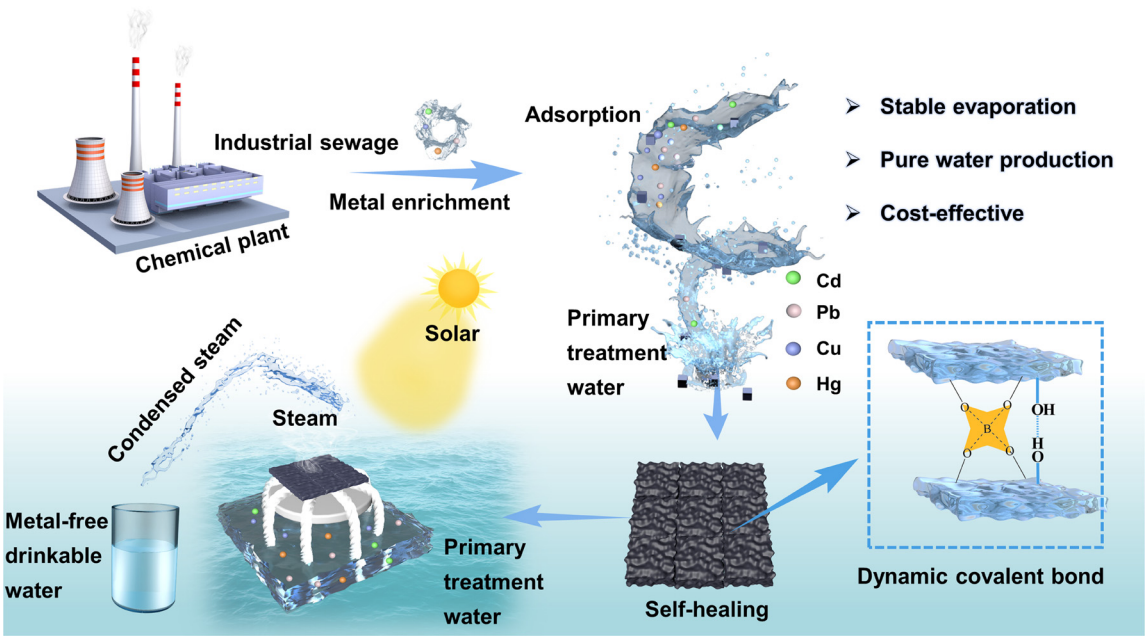

Fig. 1 Schematic illustration of solar water purification using CPPB gel.

wastewater into heavy-metal-free drinking water. An evaporator prepared by combining the self-healing gel with cotton thread achieved a high steam purification rate of 2.19 kg m^{-2} h^{-1} under illumination by sunlight in various harsh environments. The super-stable and damage-resistant wastewater treatment system exhibits great potential for different communities to meet the demand for water in both quantity and quality.

2. Experimental

2.1 Materials fabrication

Preparation of C-CNC–PANI. Firstly, a suspension of 0.1 wt% C-CNC was dissolved in water and placed into an ice bath. When the temperature was stable, 4.9 ml aniline was dissolved in hydrochloric acid (100 ml 1 M) and added into the prepared suspension of C-CNC. After 1 hour in an ice bath, 2.5 g ammonium persulfate was dissolved in 100 ml hydrochloric acid and added into the prepared solution for 4 hours. The precipitate was then repeatedly washed with deionized water and the unreacted chemicals are removed by centrifugation with deionized water. Finally, the washed samples were freeze-dried, and the final product C-CNC–PANI was obtained.

Fabrication of CPPB hydrogel. 1.5 g PVA was added into 10 ml water solution and stirred at 90 °C for 1 hour to obtain a transparent PVA solution. Subsequently, we prepared a C-CNC–PANI suspension by dispersing C-CNC–PANI powder in an aqueous solution for 40 minutes, employing varying weight percentages (0%, 1%, 3%, 5%, and 8%) in water. This suspension was then introduced into a polyvinyl alcohol (PVA) solution and agitated at 90 °C for one hour. Following this step, we prepared different borax solutions with varying weight percentages (0.5%, 1%, 3%, 5%, and 8%) in water and added them to the suspension. The resulting mixture promptly underwent gelation, yielding a series of C-CNC–PANI–PVA–Borax hydrogels, hereinafter referred to as CPPB hydrogels.

2.2 Adsorption of heavy metal ions from simulated real wastewater

Chopped C-CNC–PANI–PVA–borax (CPPB) gel and a simulated real wastewater solution containing heavy metal ions, methylene blue (MB) and methyl orange (MO) were introduced into a plastic centrifuge tube, followed by thorough agitation in a water bath for a duration of 2 hours. Then, the supernatant was collected using a 0.22 μm filter membrane. The ion concentrations in the various water samples were measured using an inductively coupled plasma emission spectrometer (ICP-OES, Agilent 5110, Agilent Technologies, Inc., USA). The residual dye content in the solution was determined using an infrared atomic absorption spectrophotometer.

2.3 Solar steam generation

After the evaporator was prepared, the steam-generation experiments were performed under practical conditions with a homemade optical system, with a xenon lamp solar simulator as the light source (AM 1.5G filter, CEL-HXF300, Beijing Taught Jinyuan technology Co.). Additionally, the output power underwent independent calibration through an optical power meter (CEL-NP2000, Beijing Taught Jinyuan Technology Co.). The water evaporation experiment was conducted in a 50 mL crystallizing dish filled with 30 mL of primary treatment water, followed by irradiation under a solar simulator emitting 100 mW cm^{-2}. All experiments were carried out at room temperature (25 °C) with an approximate humidity level of 50%. During the experiment, changes in the system's mass were quantified using an electronic balance, while real-time temperature variations were monitored *via* infrared cameras. Collected water subjected to the evaporation process was tested for heavy metal ion concentrations as a means of assessing the wastewater purification efficacy.

3. Result and discussion

3.1 Hydrogel preparation, morphology and component analysis

Polyvinyl alcohol (PVA), a water-soluble synthetic polymer, has drawn considerable attention as an optimal material for many polymer composite materials owing to its pronounced hydrophilicity, favorable biocompatibility, biodegradability, exceptional mechanical strength, and effortless processability.[38] Therefore, we incorporated it as the foundational material for the gel. PANI has been utilized as a model for photothermal nanomaterials owing to its cost-effectiveness and broad/high light absorption capacity.[39,40] However, the tendency to aggregate can compromise light management, such as light absorption and scattering, resulting in a decreased efficiency of solar-to-thermal energy conversion.[41] Therefore, the preparation of highly dispersed PANI with uniform nanostructure can facilitate solar absorption and energy confinement.[42] In the presence of C-CNC templates, the growth of PANI occurred along with C-CNC for the formation of a composite material known as C-CNC–PANI. The aggregation problem of polyaniline was solved by introducing C-CNC as the growth template. Upon mixing PVA with C-CNC–PANI, as depicted in Fig. 2a, and gradually adding a borax solution dropwise, numerous dynamic covalent and non-covalent bonds form resulting in the rapid gelation of the mixture, therefore generating a C-CNC–PANI–PVA–borax gel (CPPB gel for short). CPPB gel images of loaded and unloaded C-CNC–PANI are shown in Fig. 2e. In order to substantiate the successful loading of polyaniline (PANI), a comprehensive analysis of C-CNC–PANI was conducted, which included scanning electron microscopy (SEM), transmission electron microscopy (TEM), TEM-mapping, Fourier-transform infrared spectroscopy (FTIR), and zeta potential analysis. The results presented in Fig. S1† indicate that the surface of C-CNC is smooth. Upon loading with PANI, SEM imaging reveals the presence of nanorods on the surface of C-CNC–PANI, confirming that PANI was used as a growth template during the fabrication

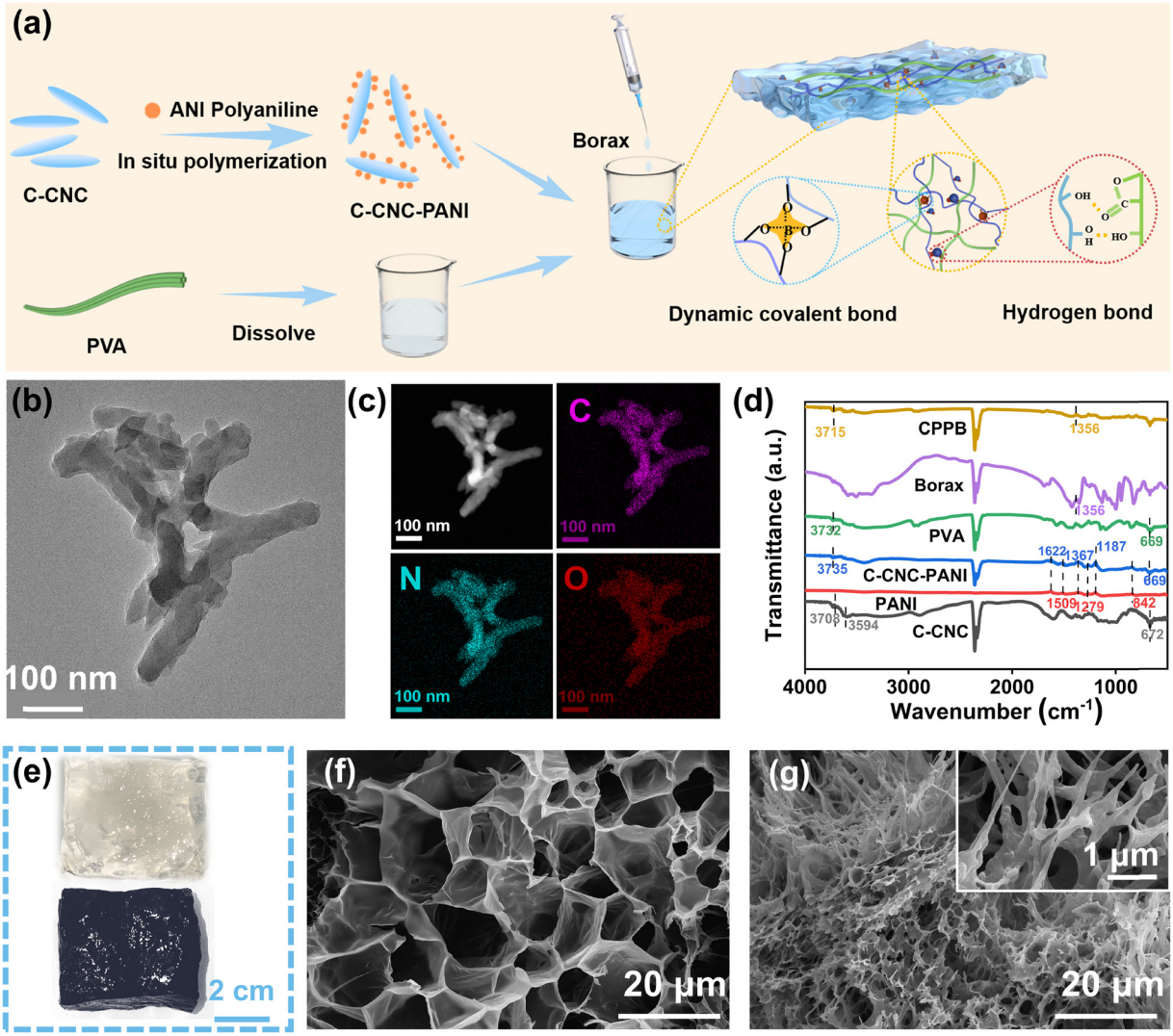

Fig. 2 Fabrication and characterizations of CPPB gels. (a) Schematic illustration of the preparation process of CPPB gels. (b) TEM image of C-CNC–PANI. (c) TEM mapping of C-CNC–PANI. (d) FTIR. (e) Photo of the CCPB gels containing unloaded C-CNC–PANI and loaded C-CNC–PANI. (f) SEM image of the CPPB gels unloaded C-CNC–PANI. (g) SEM image of the CPPB gels loaded C-CNC–PANI.

process. It is evident from the transmission electron microscopic (TEM) image presented in Fig. 2b that polyaniline (PANI) exhibits excellent dispersion properties. This is further supported by the elemental analysis, which reveals that the unique C element in the C-CNC and the unique N element in PANI are both evenly distributed throughout the sample (Fig. 2c). The spectral analysis of the C-CNC–PANI composite, as obtained from FTIR (Fig. 2d), reveals significant similarities with pristine PANI, thereby confirming the successful polymerization of PANI and C-CNC. Notably, the initial zeta potential of C-CNC was negative, in contrast to the positive zeta potential of PANI (Fig. S2†). This observation indicates that the electrostatic interaction between C-CNC and PANI has significantly enhanced the dispersion of PANI. These findings validate the successful loading of PANI onto C-CNC. Moreover, the gel characterization of the C-CNC–PANI loading before and after was performed using SEM. The gel before loading (Fig. 2f) displayed a porous structure, while after the loading of C-CNC–PANI, the gel surface showed the presence of fine fibers, (Fig. 2g) indicating the successful loading and dispersion of C-CNC–PANI in the CPPB gel. Fig. 2d illustrates the chemical structure and the dynamic hydrogen bonding within the hydrogel. In the FTIR spectrum, the CPPB gel displays a peak shift toward lower wavenumbers when compared to C-CNC and PVA. Notably, the peaks observed at approximately 3735 cm^{-1} (C-CNC–PANI) and 3732 cm^{-1} (PVA) undergo a subtle shift to a lower wavenumber of 3715 cm^{-1}, which can be attributed to the formation of hydrogen bonds involving PVA chains, C-CNC–PANI, and intermolecular bonding (H-bonds). Additionally, the peak at 1356 cm^{-1} indicates the presence of borate species, signifying the asymmetric stretching and relaxation of B–O–C bonds. These observations provide strong evidence for the existence of dynamic borate ester bonds and hydrogen bonds within the CPPB hydrogel.[42]

To determine the minimum concentration of borax required for the gelation of composite hydrogels, varying ratios of borax were added to a mixture of PVA and C-CNC–PANI. As shown in Fig. S3,† low concentrations of borax (*e.g.* 0.5, 1 wt%) failed to initiate the sol–gel transition, resulting in a flow state of the PVA and the C-CNC–PANI mixture. As the concentration of borax increased, complete gelation was gradually achieved, and the self-healing properties of the CPPB gels containing different amounts of borax were tested (Fig. S4†). It was found that the self-healing performance became stable when the borax concentration reached 3 wt% (since the 0.5 wt% CPPB gel did not undergo gelation, self-healing could not be observed).

After determining the optimal ratio of borax, the proportion of C-CNC–PANI was adjusted. Different proportions of C-CNC–PANI were mixed with PVA and 3 wt% of borax was added. As shown in Fig. S5,† CPPB gels could be gelled when the proportion of C-CNC–PANI was less than 3 wt%, but incomplete gelation occurred when the proportion of C-CNC–PANI was increased to a higher level (such as 5, 8 wt%). Self-healing tests were performed on CPPB gels containing different amounts of C-CNC–PANI, and it was found that 3 wt% exhibited the best self-healing performance (Fig. S6†). Therefore, 3 wt% was determined as the optimal amount of C-CNC–PANI in CPPB gels.

3.2 Self-healing performance of CPPB hydrogel

After determining the optimal and ideal ratios of C-CNC–PANI to borax, a CPPB gel was prepared and the self-healing performance of the CPPB gel containing 3 wt% C-CNC–PANI and 3 wt% borax was evaluated (all subsequent experiments were conducted based on this ratio). Fig. 3a illustrates the self-healing process of CPPB gel under various environmental conditions. When the separated gels come into contact under an ambient atmosphere, the edges fuse together, and over time, the gap gradually disappears. It is noteworthy that the gel can achieve self-healing not only in air and water environments but also in harsh conditions such as pH 1 and pH 11. Considering practical applications, we also examined the self-healing behavior in wastewater, dyes (methylene blue and methyl orange), and saline water, and found that its self-healing performance was stable. Furthermore, the healed gel exhibits the ability to withstand stretching in different directions without undergoing disintegration (Videos S1, ESI†). The self-healing mechanism of the hydrogels is illustrated in Fig. 3b and c. Borax dissolves rapidly in water generating trigonal planar boric acid $B(OH)_3$ and tetrahedral borate ions $B(OH)_4^-$. This reaction is reversible, and the two substances exchange rapidly in solution. $B(OH)_4^-$ can easily form multiple coordination bonds with two adjacent hydroxyl groups of PVA chains using the *cis*-diol sites, thereby forming dynamic borate ester bonds. These dynamic chemical bonds constitute the main linkages of the hydrogel network. The entanglement of the polymer chains, dynamic borate ester bond formation, as well as intramolecular and intermolecular hydrogen bonding, constitute the dynamic reversible network, providing excellent self-healing properties for the hydrogels.[43] Optical microscopic images of the CPPB gels self-healing process are depicted in Fig. 3d, confirm the gradual healing of separated gels, facilitated by dynamic covalent bonds

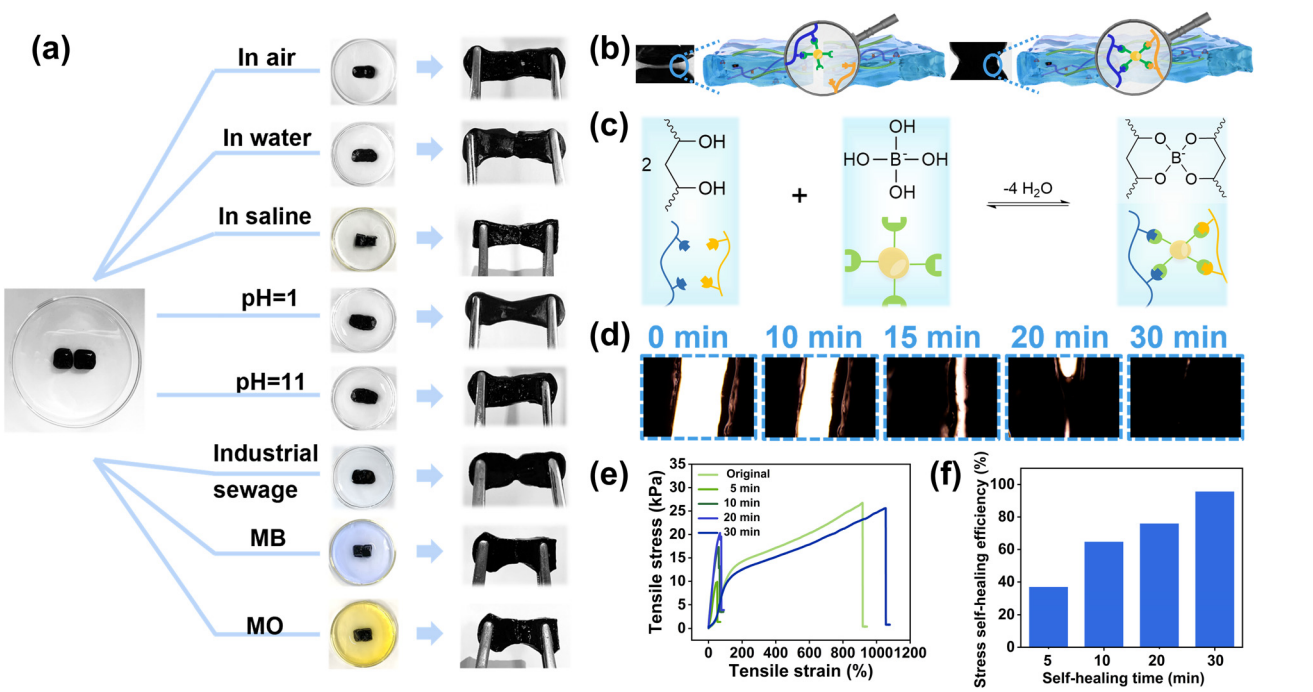

Fig. 3 Self-healing properties of CPPB hydrogel. (a) Photographs of the self-healing properties of CPPB gels under varying environmental conditions. (b) Illustration depicting the self-healing properties of a gel. (c) The mechanism of the self-healing gel. (d) Optical microscopic images. (e) Tensile stress–strain curves under different self-healing time. (f) Diagram depicting the efficiency of self-healing.

(Videos S2, ESI†). It is noteworthy that complete healing was achieved within 30 minutes. The mechanical properties of the gels before and after healing were elucidated through a series of tensile experiments (Fig. S7a†). Initially, tensile testing was conducted on CPPB gel specimens with varying ratios of C-CNC–PANI, yielding stress–strain curves for five distinct samples. As the ratio of C-CNC–PANI increased, the tensile strength of the hydrogel, which is the maximum stress the hydrogel can withstand before breaking, increased (Fig. S7b†). This phenomenon is consistent with the design of a synergistic soft–hard hierarchical network. The PVA polymer chain, serving as the pliable matrix, and the C-CNC–PANI cellulose nanocrystals, functioning as the nano-sized reinforcing domains, collaboratively create a layered "soft–hard" network structure characterized by a diverse array of intermolecular hydrogen bonds. The extensive intermolecular hydrogen bonds between the soft matrix and the hard nano-sized reinforcing domain contribute to maintaining the integrity of the entire layered network structure, thus enhancing the mechanical properties of the CPPB gels.[44] To further evaluate the self-healing ability, the mechanical properties of the CPPB containing 3 wt% C-CNC–PANI hydrogels after different self-healing times were characterized using the tensile test (Fig. 3e). Results indicated that the tensile strength of the self-healed gel gradually increased over time, with a significant improvement observed after 30 minutes of self-healing, leading to a substantial restoration of its mechanical performance. The self-healing efficiency, a critical parameter for evaluating the self-healing ability, is calculated using eqn (S1) (ESI†), and the corresponding results are depicted in Fig. 3f. As the healing time is prolonged, the tensile strength and strain gradually increase, and the dynamic covalent bonds are reconstructed, resulting in the restoration of the mechanical performance, which is almost fully recovered after 30 minutes of healing. The self-healing efficiency can reach as high as 95.66%.

3.3 Heavy metal ions adsorption and exhausted absorbents upcycled for evaporators

The CPPB gel contains abundant hydroxyl/carboxyl groups, which can be used to enrich toxic heavy metal ions, such as Pb^{2+}, Cu^{2+}, Cd^{2+}, and Hg^{2+}. The strong binding between metal ions and hydroxyl/carboxyl groups, ensures that toxic metal ions from wastewater are enriched in the network structure of the CPPB gels. To further explore the feasibility of its practical application in metal ion enrichment, a two-step water purification process of adsorption and evaporation was designed to purify wastewater, and the wastewater treatment

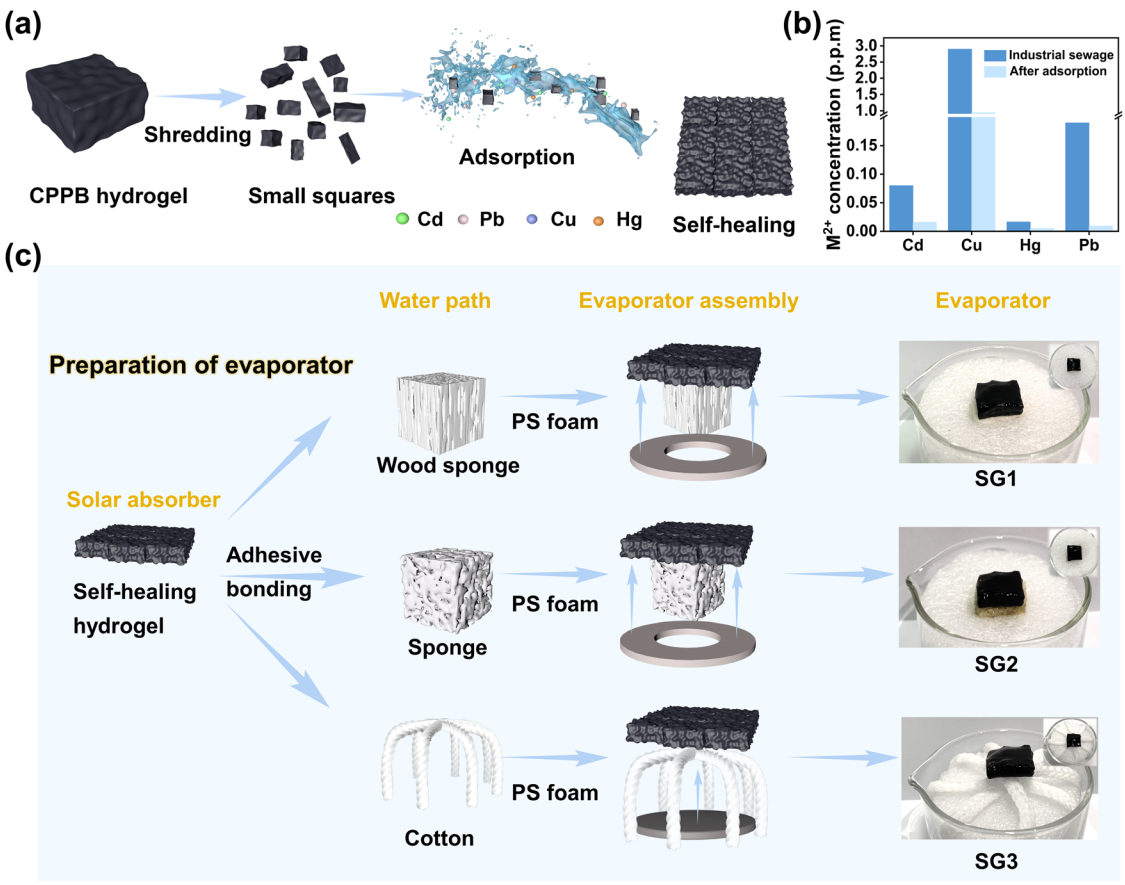

Fig. 4 Wastewater disposal and evaporator preparation. (a) Diagram depicting the adsorption of CPPB gels. (b) Concentration of heavy metal ions following the process of adsorption. (c) Schematic diagram of the fabrication of interfacial steam generation systems.

performance was evaluated using simulated wastewater (Table S1, ESI†). The adsorption process is shown in Fig. 4a, in which the CPPB gel was cut into small squares and added to the simulated wastewater for adsorption with shaking. After 2 hours, most of these heavy metal ions were adsorbed and enriched in the gel, resulting in lighter color and a decrease of heavy metal ions by 1–2 orders of magnitude (Fig. 4b). In addition to its remarkable self-healing ability, the CPPB gel demonstrates commendable self-adhesive properties, enabling it to conform to diverse non-linear surfaces. Notably, it adheres effectively to the surfaces of wood sponge, commercial sponge, and hydrophilic cotton threads within 2–3 minutes of contact, as depicted in Fig. S8.† A result of the good self-adhesive properties, the hydrogel is combined with wood sponge, commercial sponge, and hydrophilic cotton fabric to form three different evaporators. Wood sponge, commercial sponge and hydrophilic cotton fabric serve as water transport pathways, and circular polystyrene foam (PS foam) is used as a thermal barrier, providing sufficient support to keep the entire evaporator structure isolated on the water surface (Fig. 4c).

3.4 Solar driven water evaporation

The solar evaporative performance of the CPPB evaporator was evaluated using carefully designed equipment, as shown in Fig. 5a and the physical image is presented in Fig. S9.† The effect of different C-CNC–PANI doping ratios on the solar steam evaporation performance was investigated using SG1 evaporator, as depicted in Fig. S10a and b.† As the doping ratio increased gradually, the water evaporation rate also increased. However, when the doping ratio exceeded 3 wt%, the water evaporation rate decreased. Based on the gelation degree, self-healing performance, mechanical properties, and photothermal performance, 3 wt% was identified as the optimal doping ratio for the CPPB gel and was used for all subsequent tests. In terms of optical performance, as demonstrated in Fig. 5b, CPPB gel exhibits excellent absorbance of approximately 98.50% within a wide wavelength range from 250–2500 nm, with a primary absorption loss of approximately 1.50% attributed to reflectance (Fig. S11b†). This is because the detected transmittance is almost negligible (Fig. S11a†). Subsequently, the CPPB gel was placed on top of bulk water for solar-driven water evaporation. The photothermal behavior was evaluated by monitoring the temperature changes on the surfaces of the three evaporators under sunlight, as illustrated in Fig. 5c. The surface temperatures of SG1–SG3 evaporators rapidly increased within 12 min when exposed to the simulated sunlight (1 kW m^{-2}) (SG3 showed the most significant increase, rising from 14.8 °C to 34.7 °C) and stabilizing

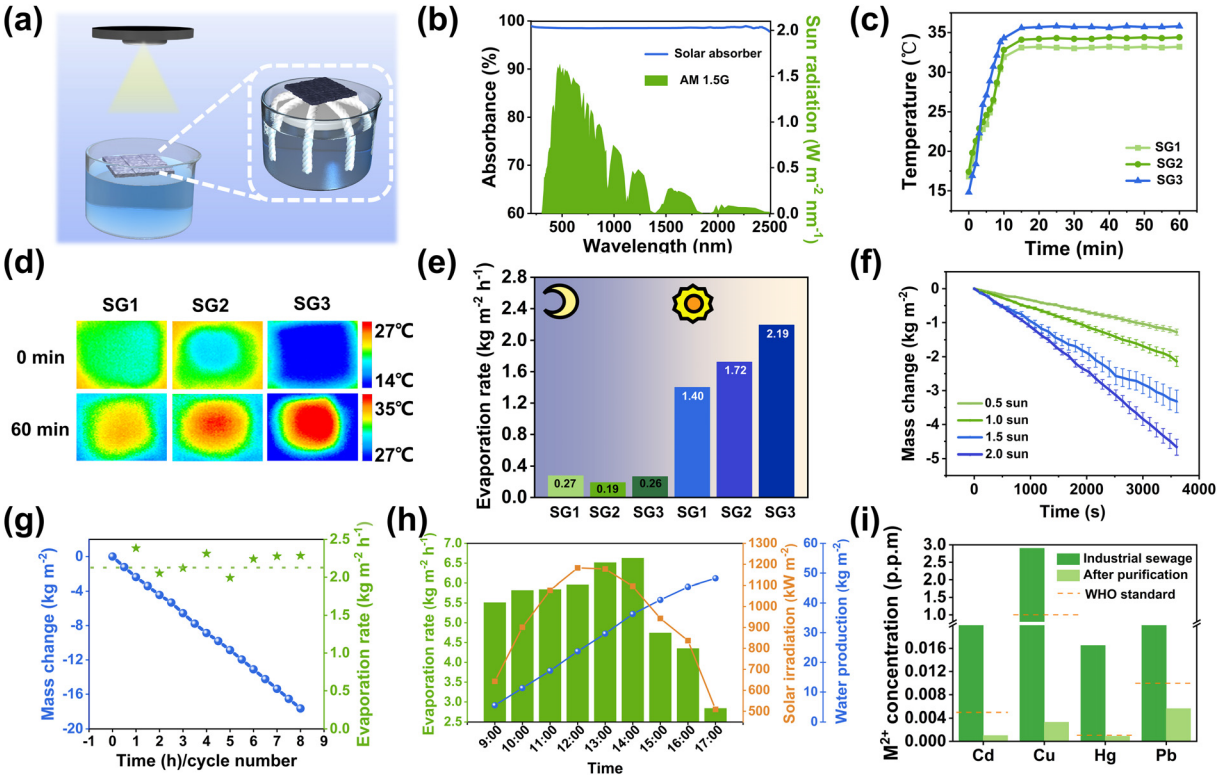

Fig. 5 Solar evaporation characterization. (a) Schematic of the interfacial steam generator SG3. (b) UV-vis-NIR absorption spectrum of the CPPB gel. (c) The temperatures at interfacial steam generators surface under one sun irradiation. (d) The corresponding infrared images of the temperature distribution over time under 1 sun. (e) Water evaporation rates in dark and light conditions. (f) Mass change of water from SG3 under 0.5–2 sun. (g) Durability testing: continuous 8 hour and repetition for 8 cycles. (h) Variation curve of sunlight intensity and evaporation rate in a day. (i) The overall heavy metal removal performance of SG3 before and after solar distillation.

between 15 and 60 minutes (SG3 remained stable at around 35.8 °C), as shown in Fig. 5d. In addition, the introduction of a substrate with a lower thermal conductivity is crucial for thermal localization, with the thermal conductivity of the cotton thread being 0.28 W m^{-1} K^{-1} (Table S2†). In order to measure the rate of water evaporation, the loss of water over time was recorded (Fig. S12†).

When exposed to one sunlight, it is evident that the evaporation rate of SG3 is faster than SG1 and SG2, as indicated by the significant decrease in water quantity. As illustrated in Fig. 5e, the rate of water evaporation in SG3 was measured as 2.19 kg m^{-2} h^{-1}, which is superior to SG1 (1.40 kg m^{-2} h^{-1}) and SG2 (1.72 kg m^{-2} h^{-1}). The evaporation efficiency of CPPB is calculated as 86.93% (calculated using eqn (S7)–(12), ESI†).[13] To investigate the water transport capabilities of the substrates, tests were performed for the three types of evaporators. The water transport capabilities were characterized by the half-swelling time, water transmission rate, and saturated water content. The saturation water content (Qs) of the three evaporators was determined through expansion tests (calculated using eqn (S3), ESI†). It was found that SG3 reached the saturated water state in 15 minutes, and that the Qs of SG3 was 6.92 g (Fig. S13a†). Dynamic analysis of the expansion behavior of SG3 enabled the calculation of the water transport rate (calculated using eqn (S4), ESI†). The SG3 water transport rate was found to be 0.46 g min^{-1}, as shown in Fig. S13b,† far superior to SG1 and SG2, and is the main reason for the difference in water evaporation rates. Consequently, all subsequent tests were conducted using SG3. To comprehensively assess the efficacy of the CPPB evaporation system in solar steam generation under 1.0 sun, a detailed analysis was performed to compare the system's heat loss and energy gain (calculated using eqn (S5) and (S6), ESI†).[45] The results indicated that, the top and side energy losses of the CPPB evaporative system were calculated to be 0.0873 W, while the environmental energy gain, attributed to the lower temperature of the cotton thread compared to the ambient temperature, was 0.123 W. This net effect of the disparity confirms a significant energy gain of 0.0357 W from the environment, effectively enhancing the overall water evaporation rate of the system. Furthermore, investigations were conducted on the evaporation rate of SG3 under varying intensities of incident light. Specifically, the evaporation rate of SG3 was measured at 0.5, 1, 1.5, and 2 sunlight intensities, resulting an evaporation rate of 1.27, 2.19, 3.32, and 4.67 kg m^{-2} h^{-1}, respectively (Fig. 5f). To validate the stability of the evaporator's performance, continuous 8 hour experiments and 8 repeated trials were performed. The experiments recorded the linear mass loss of water within 8 hours and the evaporation rate for each of the 8 repeated trials. The results indicate that the evaporation rates across the 8 trials closely align with the average evaporation rate observed over 8 hours, demonstrating minimal variance (Fig. 5g). The research findings indicate that SG3 exhibits high efficiency and stability in its solar-powered water evaporation capabilities. To confirm the stability of the structure, SEM images of the hydrogel before and after the cycling were examined. The porous structure of the hydrogel before and after evaporation shows negligible changes, thereby further validating the stability of the evaporator (Fig. S14†).

To further demonstrate the actual evaporation performance of the evaporator, an outdoor experiment was conducted on May 22, 2023, in Baoding (Baoding, China, Longitude: 115.46481 E, Latitude: 38.873891 N, temperature of around 32 °C with 22% humidity, and level 4 Southwest wind with a speed range of 5.5–7.9 m s^{-1}) (Fig. S15†). The corresponding incident solar intensity and water evaporation rate are shown in Fig. 5h. The cumulative water production from the device from 9:00 am to 5:00 pm was 48.23 kg m^{-2}, exceeding the daily outdoor evaporation capacity of current reported evaporators that can meet the normal needs of more than 10 people.[46,47] The maximum evaporation rate in outdoor water purification processes reaches 6.63 kg m^{-2} h^{-1}, which is significantly higher than the evaporation rate under one sun during laboratory experiments. This outstanding outdoor evaporation rate can be attributed to two factors. Firstly, outdoor temperatures are much higher than indoor temperatures during the summer.[48] The variation in the incident angle of outdoor sunlight resulted in a high evaporation rate of 6.63 kg m^{-2} h^{-1}. It is noteworthy that both the surface and sides of the evaporator serve as areas conducive to evaporation. Secondly, in the context of the outdoor experiment, the surface of the evaporator is effectively cooled by the flow of air.[49] The elevated outdoor temperature and airflow contribute to increased efficiency. Outdoor winds enhance efficiency by cooling the evaporator's evaporation surface, maintaining an unsaturated state that boosts the evaporator's evaporation rate. As such, the high-humidity air present on the evaporator surface is consistently replaced with air having low humidity. This phenomenon creates an unsaturated environment on the surface of the evaporator and consequently results in a significant improvement in the efficiency of evaporation.[50]

Due to the complexity of the application environment for solar-driven water evaporation, the stable operation of the evaporator under harsh conditions is crucial. Therefore, the water evaporation rate of the evaporator in artificially salted water of different concentrations, saline, strong acid (pH = 1), and strong alkali (pH = 11), were determined as shown in Fig. S16–S18.† The water evaporation rate shows no significant decrease compared to that in pure water, and in the strong acid and strong alkali environment, the collected pure water is purified to a neutral condition, verifying the high-efficiency in complex environments. To confirm the feasibility of the SG3 evaporator for purifying wastewater, the adsorbed water underwent further distillation treatment using the SG3 evaporator. Only partial removal of heavy metal ions is achieved through the solar interfacial evaporation process, which fails to meet World Health Organization (WHO) drinking water standards (Fig. S19†).[7] Therefore, a two-step purification approach involving adsorption and evaporation was employed. As shown in Fig. 5i, after two rounds of adsorption–evaporation

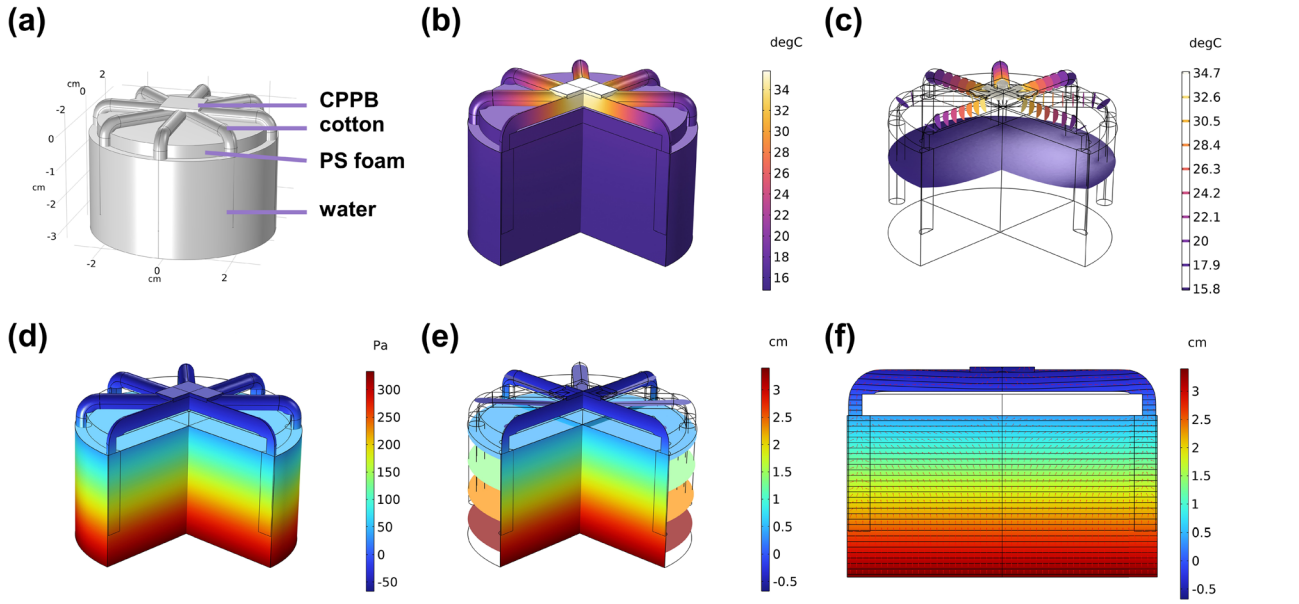

Fig. 6 Theoretical simulation of solar vapor generation of SG3 evaporator under one sun illumination. (a) SG3 evaporator model diagram. Steady-state simulation of (b) temperature, (c) temperature isosurface, (d) relative water pressure, (e) hydraulic head isosurface and (f) hydraulic head distribution.

purification, the concentration of heavy metal ions decreased by 3–6 orders of magnitude and the concentration of the four heavy metal ions in the collected water was much lower than the drinking water standard defined by the WHO. In addition, the concentration of mercury ions was already significantly lower than the WHO drinking water standard after the adsorption process, and there was no significant change in the concentration of mercury ions after further evaporation purification, indicating that the evaporation process made little contribution to the further removal of mercury.[7,51] Furthermore, the loss of the water was recorded during the wastewater evaporation treatment process, which was almost the same as that of pure water (Fig. S20†). The overall purification performance of the evaporator suggests that it exhibits significant potential for the removal of heavy metal ions and wastewater purification. Moreover, when using methylene blue (MB) and methyl orange (MO) dyes as organic pollutants from industrial wastewater, as shown in Fig. S21 and S22.† The adsorption process resulted in a notable decrease in the color of the solution. Following the purification process of adsorption–evaporation, the solution became colorless, and the strong absorption peaks of MB (≈665 nm) and MO (≈465 nm) were completely eliminated in the condensed water, indicating the excellent water purification ability of the evaporator.

3.5 Theoretical calculations for solar vapor generation of SG3 evaporator

To further clarify and understand the heat transfer process and water transport in the SG3 evaporator in real application scenarios, a simulation was conducted using COMSOL Multiphysics.[52,53] Initially, a model of the SG3 evaporator immersed in water under solar radiation was created with the same size parameters (Fig. 6a). The temperature distribution and cross-sectional views are shown in Fig. 6b, c, S23 and S24† with the surface temperature quickly reaching around 35 °C. The simulated top surface temperature matches well with the experimental results. The evaporator demonstrates good thermal localization, as the heat from the evaporative surface can only be transferred over a short distance, reducing heat diffusion into the bulk water and promoting the efficiency of solar energy conversion to steam. Fig. 6d, e, S25 and S26† illustrate the simulated distribution of relative water pressure, indicating that negative relative pressure is formed on the gel surface as steam is generated, ensuring continuous water delivery. Fig. 6f and S27† shows the distribution of simulated hydraulic head and Darcy velocity field, further confirming the continuous water flow generated through capillary core suction and water evaporation, delivering water along the cotton thread to the gel, enabling efficient water delivery to compensate for surface water loss. The calculations demonstrate that the fabricated evaporator upcycled by exhausted adsorbents shows great potential in practical water purifications.

4. Conclusions

In this study, we have developed a wastewater purification system with outstanding water purification capabilities under complex environmental conditions, exhibiting exceptional durability for stable and highly efficient continuous drinking water generation. In particular, the cotton thread evaporator achieves a high evaporation rate of up to 2.19 kg m^{-2} h^{-1} under sunlight, as well as a continuous outdoor evaporation quantity of 48.23 kg m^{-2} over 8 hours, confirming its great

potential in practical applications. The adsorption-evaporation purification process ensures that the wastewater purification aligns with the drinking water standards established by the WHO. This highly efficient wastewater purification system exhibits excellent long-term stability and energy-saving characteristics, providing an efficient, green, and sustainable route for wastewater regeneration.

Author contributions

Meng Li: visualization, methodology, conceptualization. Hongmin Guo: conceptualization, writing – original draft, investigation, formal analysis. Yumeng Xiao: investigation. Sichen Liu: software. Yifan Lu: formal analysis. Lidong Wang: project administration, writing – review & editing. Tony D. James: visualization, project administration, writing – review & editing.

Conflicts of interest

The authors declare no competing interests.

Acknowledgements

This research is supported by the National Natural Science Foundation of China (No. 52370110), and the Fundamental Research Funds for the Central Universities (No. 2023MS146). TDJ wishes to thank the University of Bath and the Open Research Fund of the School of Chemistry and Chemical Engineering, Henan Normal University (2020ZD01) for support.

References

1 N. Li, L. Qiao, J. He, S. Wang, L. Yu, P. Murto, X. Li and X. Xu, Solar-Driven Interfacial Evaporation and Self-Powered Water Wave Detection Based on an All-Cellulose Monolithic Design, *Adv. Funct. Mater.*, 2020, **31**, 2008681.
2 M. Gao, L. Zhu, C. K. Peh and G. W. Ho, Solar absorber material and system designs for photothermal water vaporization towards clean water and energy production, *Energy Environ. Sci.*, 2019, **12**, 841–864.
3 N. Mahesh, S. Balakumar, S. Shyamalagowri, J. Manjunathan, M. K. S. Pavithra, P. S. Babu, M. Kamaraj and M. Govarthanan, Carbon-based adsorbents as proficient tools for the removal of heavy metals from aqueous solution: A state of art-review emphasizing recent progress and prospects, *Environ. Res.*, 2022, **213**, 113723.
4 X. Min, B. Zhu, B. Li, J. Li and J. Zhu, Interfacial Solar Vapor Generation: Materials and Structural Design, *Acc. Mater. Res.*, 2021, **2**, 198–209.
5 C. He, Z. Liu, J. Wu, X. Pan, Z. Fang, J. Li and B. A. Bryan, Future global urban water scarcity and potential solutions, *Nat. Commun.*, 2021, **12**, 4667.
6 X. Wu, Z. Wu, Y. Wang, T. Gao, Q. Li and H. Xu, All-Cold Evaporation under One Sun with Zero Energy Loss by Using a Heatsink Inspired Solar Evaporator, *Adv. Sci.*, 2021, **8**, 2002501.
7 Y. Guo, H. Lu, F. Zhao, X. Zhou, W. Shi and G. Yu, Biomass-Derived Hybrid Hydrogel Evaporators for Cost-Effective Solar Water Purification, *Adv. Mater.*, 2020, **32**, 1907061.
8 M. Li, M. Xu, Q. Shi, H. Wang, H. Guo, L. Wang and T. D. James, An upcycled wood sponge adsorbent for drinking water purification by solar steam generation, *Environ. Sci.: Nano*, 2022, **9**, 2559–2571.
9 M. Li, B. Liu, H. Guo, H. Wang, Q. Shi, M. Xu, M. Yang, X. Luo and L. Wang, Reclaimable MoS(2) Sponge Absorbent for Drinking Water Purification Driven by Solar Energy, *Environ. Sci. Technol.*, 2022, **56**, 11718–11728.
10 M. Li, B. Liu, Z. Liu, Y. Xiao, H. Guo, Z. An, L. Wang and T. D. James, Reducing Heat Conduction Enhances the Photothermal Efficiency of Upcycled Adsorbents, *Adv. Funct. Mater.*, 2022, **33**, 2209987.
11 C. S. Patil, A. N. Kadam, D. B. Gunjal, V. M. Naik, S.-W. Lee, G. B. Kolekar and A. H. Gore, Sugarcane molasses derived carbon sheet@sea sand composite for direct removal of methylene blue from textile wastewater: Industrial wastewater remediation through sustainable, greener, and scalable methodology, *Sep. Purif. Technol.*, 2020, **247**, 116997.
12 A. Subash, M. Naebe, X. Wang and B. Kandasubramanian, Biopolymer – A sustainable and efficacious material system for effluent removal, *J. Hazard. Mater.*, 2023, **443**, 130168.
13 R. Niu, J. Ren, J. J. Koh, L. Chen, J. Gong, J. Qu, X. Xu, J. Azadmanjiri and J. Min, Bio-Inspired Sandwich-Structured All-Day-Round Solar Evaporator for Synergistic Clean Water and Electricity Generation, *Adv. Energy Mater.*, 2023, **13**, 2302451.
14 P. He, H. Lan, H. Bai, Y. Zhu, Z. Fan, J. Liu, L. Liu, R. Niu, Z. Dong and J. Gong, Rational construction of "all-in-one" metal-organic framework for integrated solar steam generation and advanced oxidation process, *Appl. Catal., B*, 2023, **337**, 123001.
15 M. Li, M. Yang, B. Liu, H. Guo, H. Wang, X. Li, L. Wang and T. D. James, Self-assembling fluorescent hydrogel for highly efficient water purification and photothermal conversion, *Chem. Eng. J.*, 2022, **431**, 134245.
16 L. Li, J. Zhu and Z. Zeng, New Approach for Recycling Office Waste Paper: An Efficient and Recyclable Material for Oily Wastewater Treatment, *ACS Appl. Mater. Interfaces*, 2020, **12**, 55894–55902.
17 P. V. Devre, A. S. Patil, D. Sohn and A. H. Gore, Upcycling of spent granular carbon into sustainable and recyclable biopolymeric hybrid hydrogel for highly efficient adsorptive removal of tetracycline pollutant from environmental waters and industrial effluents, *J. Environ. Chem. Eng.*, 2023, **11**, 109368.
18 F. Li, N. Li, S. Wang, L. Qiao, L. Yu, P. Murto and X. Xu, Self-Repairing and Damage-Tolerant Hydrogels for Efficient Solar-Powered Water Purification and Desalination, *Adv. Funct. Mater.*, 2021, **31**, 2104464.
19 H. Lu, M. Li, X. Wang, Z. Wang, M. Pi, W. Cui and R. Ran, Recyclable physical hydrogels as durable and efficient solar-driven evaporators, *Chem. Eng. J.*, 2022, **450**, 138257.

20 Q. Ling, W. Liu, J. Liu, L. Zhao, Z. Ren and H. Gu, Highly Sensitive and Robust Polysaccharide-Based Composite Hydrogel Sensor Integrated with Underwater Repeatable Self-Adhesion and Rapid Self-Healing for Human Motion Detection, *ACS Appl. Mater. Interfaces*, 2022, **14**, 24741–24754.

21 Y. Wang, P. Chen, X. Zhou, Y. Liu, N. Wang and C. Gao, Highly Sensitive Zwitterionic Hydrogel Sensor for Motion and Pulse Detection with Water Retention, Adhesive, Antifreezing, and Self-Healing Properties, *ACS Appl. Mater. Interfaces*, 2022, **14**, 47100–47112.

22 Y. Chen, Y. Zheng, Y. Zhou, W. Zhang, W. Li, W. She, J. Liu and C. Miao, Multi-layered cement-hydrogel composite with high toughness, low thermal conductivity, and self-healing capability, *Nat. Commun.*, 2023, **14**, 3438.

23 T. Magrini, F. Bouville, A. Lauria, H. Le Ferrand, T. P. Niebel and A. R. Studart, Transparent and tough bulk composites inspired by nacre, *Nat. Commun.*, 2019, **10**, 2794.

24 Z. Wei, J. H. Yang, Z. Q. Liu, F. Xu, J. X. Zhou, M. Zrínyi, Y. Osada and Y. M. Chen, Novel Biocompatible Polysaccharide-Based Self-Healing Hydrogel, *Adv. Funct. Mater.*, 2015, **25**, 1352–1359.

25 Z. Wei, J. H. Yang, J. Zhou, F. Xu, M. Zrinyi, P. H. Dussault, Y. Osada and Y. M. Chen, Self-healing gels based on constitutional dynamic chemistry and their potential applications, *Chem. Soc. Rev.*, 2014, **43**, 8114–8131.

26 Y. Chen, A. M. Kushner, G. A. Williams and Z. Guan, Multiphase design of autonomic self-healing thermoplastic elastomers, *Nat. Chem.*, 2012, **4**, 467–472.

27 J. Chen, Y. Gao, L. Shi, W. Yu, Z. Sun, Y. Zhou, S. Liu, H. Mao, D. Zhang, T. Lu, Q. Chen, D. Yu and S. Ding, Phase-locked constructing dynamic supramolecular ionic conductive elastomers with superior toughness, autonomous self-healing and recyclability, *Nat. Commun.*, 2022, **13**, 4868.

28 H. Guo, Y. Han, W. Zhao, J. Yang and L. Zhang, Universally autonomous self-healing elastomer with high stretchability, *Nat. Commun.*, 2020, **11**, 2037.

29 S. Wang and M. W. Urban, Self-healing polymers, *Nat. Rev. Mater.*, 2020, **5**, 562–583.

30 Y. Zhao, Y. Ohm, J. Liao, Y. Luo, H.-Y. Cheng, P. Won, P. Roberts, M. R. Carneiro, M. F. Islam, J. H. Ahn, L. M. Walker and C. Majidi, A self-healing electrically conductive organogel composite, *Nat. Electron.*, 2023, **6**, 206–215.

31 J. Yin, C. Lu, C. Li, Z. Yu, C. Shen, Y. Yang, X. Jiang and Y. Zhang, A UV-filtering, environmentally stable, healable and recyclable ionic hydrogel towards multifunctional flexible strain sensor, *Composites, Part B*, 2022, **230**, 109528.

32 J. Chen, M. Jian, X. Yang, X. Xia, J. Pang, R. Qiu and S. Wu, Highly Effective Multifunctional Solar Evaporator with Scaffolding Structured Carbonized Wood and Biohydrogel, *ACS Appl. Mater. Interfaces*, 2022, **14**, 46491–46501.

33 S. Chaule, J. Hwang, S. J. Ha, J. Kang, J. C. Yoon and J. H. Jang, Rational Design of a High Performance and Robust Solar Evaporator via 3D-Printing Technology, *Adv. Mater.*, 2021, **33**, e2102649.

34 X. Zheng, Y. Bao, A. Huang, G. Qin and M. He, 3D printing double-layer hydrogel evaporator with surface structures for efficient solar steam generation, *Sep. Purif. Technol.*, 2023, **306**, 122741.

35 N. Liu, L. Hao, B. Zhang, R. Niu, J. Gong and T. Tang, Rational Design of High-Performance Bilayer Solar Evaporator by Using Waste Polyester-Derived Porous Carbon-Coated Wood, *Energy Environ. Mater.*, 2021, **5**, 617–626.

36 X. Lin, P. Wang, R. Hong, X. Zhu, Y. Liu, X. Pan, X. Qiu and Y. Qin, Fully Lignocellulosic Biomass-Based Double-Layered Porous Hydrogel for Efficient Solar Steam Generation, *Adv. Funct. Mater.*, 2022, **32**, 2209262.

37 Q. Chen, Y. Shi, K. Sheng, J. Zheng and C. Xu, Dynamically Cross-Linked Hydrogel Electrolyte with Remarkable Stretchability and Self-Healing Capability for Flexible Electrochromic Devices, *ACS Appl. Mater. Interfaces*, 2021, **13**, 56544–56553.

38 H. Zou, X. Meng, X. Zhao and J. Qiu, Hofmeister Effect-Enhanced Hydration Chemistry of Hydrogel for High-Efficiency Solar-Driven Interfacial Desalination, *Adv. Mater.*, 2023, **35**, e2207262.

39 X. Zhao, X. Meng, H. Zou, Z. Wang, Y. Du, Y. Shao, J. Qi and J. Qiu, Topographic Manipulation of Graphene Oxide by Polyaniline Nanocone Arrays Enables High-Performance Solar-Driven Water Evaporation, *Adv. Funct. Mater.*, 2022, **33**, 2209207.

40 Z. Liu, B. Wu, B. Zhu, Z. Chen, M. Zhu and X. Liu, Continuously Producing Watersteam and Concentrated Brine from Seawater by Hanging Photothermal Fabrics under Sunlight, *Adv. Funct. Mater.*, 2019, **29**, 1905485.

41 F. Zhu, L. Wang, B. Demir, M. An, Z. L. Wu, J. Yin, R. Xiao, Q. Zheng and J. Qian, Accelerating solar desalination in brine through ion activated hierarchically porous polyion complex hydrogels, *Mater. Horiz.*, 2020, **7**, 3187–3195.

42 C. Shao, M. Wang, L. Meng, H. Chang, B. Wang, F. Xu, J. Yang and P. Wan, Mussel-Inspired Cellulose Nanocomposite Tough Hydrogels with Synergistic Self-Healing, Adhesive, and Strain-Sensitive Properties, *Chem. Mater.*, 2018, **30**, 3110–3121.

43 H. Zheng, N. Lin, Y. He and B. Zuo, Self-Healing, Self-Adhesive Silk Fibroin Conductive Hydrogel as a Flexible Strain Sensor, *ACS Appl. Mater. Interfaces*, 2021, **13**, 40013–40031.

44 Z. Ouyang, S. Cui, H. Yu, D. Xu, C. Wang, D. Tang and K. C. Tam, Versatile sensing devices for self-driven designated therapy based on robust breathable composite films, *Nano Res.*, 2021, **15**, 1027–1038.

45 L. Zhang, Z. Xu, L. Zhao, B. Bhatia, Y. Zhong, S. Gong and E. N. Wang, Passive, high-efficiency thermally-localized solar desalination, *Energy Environ. Sci.*, 2021, **14**, 1771–1793.

46 Y. Geng, W. Sun, P. Ying, Y. Zheng, J. Ding, K. Sun, L. Li and M. Li, Bioinspired Fractal Design of Waste Biomass-Derived Solar–Thermal Materials for Highly Efficient Solar Evaporation, *Adv. Funct. Mater.*, 2020, **31**, 2007648.

47 Z. Lei, S. Zhu, X. Sun, S. Yu, X. Liu, K. Liang, X. Zhang, L. Qu, L. Wang and X. Zhang, A Multiscale Porous 3D-Fabric Evaporator with Vertically Aligned Yarns Enables Ultra-

Efficient and Continuous Water Desalination, *Adv. Funct. Mater.*, 2022, **32**, 2205790.

48 C. Xu, M. Gao, X. Yu, J. Zhang, Y. Cheng and M. Zhu, Fibrous Aerogels with Tunable Superwettability for High-Performance Solar-Driven Interfacial Evaporation, *Nanomicro Lett.*, 2023, **15**, 64.

49 X. Li, M. Li, Q. Shi, H. Guo, L. Wang, X. Guo, Z. Chen, J. L. Sessler, H. Xiao and T. D. James, Exhausted Cr(VI) Sensing/Removal Aerogels Are Recycled for Water Purification and Solar-Thermal Energy Generation, *Small*, 2022, **18**, e2201949.

50 H. Li, W. Zhu, M. Li, Y. Li, R. T. K. Kwok, J. W. Y. Lam, L. Wang, D. Wang and B. Z. Tang, Side Area-Assisted 3D Evaporator with Antibiofouling Function for Ultra-Efficient Solar Steam Generation, *Adv. Mater.*, 2021, **33**, e2102258.

51 H. Y. Zhao, W. X. Dong, Y. Deng, L. F. Chen, C. F. Zhao, C. L. Zhang, J. Zhou, Y. F. Qu, Y. S. Li, D. J. Li and S. H. Yu, Biomass-based biomimetic-oriented Janus nanoarchitecture for efficient heavy-metal enrichment and interfacial solar water sanitation, *Interdiscip. Mater.*, 2022, **1**, 537–547.

52 Y. Lu, D. Fan, Y. Wang, H. Xu, C. Lu and X. Yang, Surface Patterning of Two-Dimensional Nanostructure-Embedded Photothermal Hydrogels for High-Yield Solar Steam Generation, *ACS Nano*, 2021, **15**, 10366–10376.

53 Z. Wei, C. Cai, Y. Huang, Y. Wang and Y. Fu, Biomimetic surface strategy of spectrum-tailored liquid metal via blackbody inspiration for highly efficient solar steam generation, desalination, and electricity generation, *Nano Energy*, 2021, **86**, 106138.

